MATERIALS SCIENCE

Perfect confinement of crown ethers in MOF membrane for complete dehydration and fast transport of monovalent ions

Tingting Xu[1]†, Bin Wu[2]†, Wenmin Li[1], Yifan Li[1], Yanran Zhu[1], Fangmeng Sheng[1], Qiuhua Li[3], Liang Ge[1], Xingya Li[1]*, Huanting Wang[4], Tongwen Xu[1]*

Fast transport of monovalent ions is imperative in selective monovalent ion separation based on membranes. Here, we report the in situ growth of crown ether@UiO-66 membranes at a mild condition, where dibenzo-18-crown-6 (DB18C6) or dibenzo-15-crown-5 is perfectly confined in the UiO-66 cavity. Crown ether@UiO-66 membranes exhibit enhanced monovalent ion transport rates and mono-/divalent ion selectivity, due to the combination of size sieving and interaction screening effects toward the complete monovalent ion dehydration. Specifically, the DB18C6@UiO-66 membrane shows a permeation rate (e.g., K^+) of 1.2 mol per square meter per hour and a mono-/divalent ion selectivity (e.g., K^+/Mg^{2+}) of 57. Theoretical calculations and simulations illustrate that, presumably, ions are completely dehydrated while transporting through the DB18C6@UiO-66 cavity with a lower energy barrier than that of the UiO-66 cavity. This work provides a strategy to develop efficient ion separation membranes via integrating size sieving and interaction screening and to illuminate the effect of ion dehydration on fast ion transport.

INTRODUCTION

Membrane-based selective monovalent ion separation is the crucial step for the extraction of lithium from salt brine and saline water refining (1–3). The similar hydrated ionic sizes and charges make the separation of monovalent ions from divalent ones a great challenge (4, 5). Traditional nanoporous membranes separate monovalent ions from divalent ones based on the same charge repulsion, which inhibits both the mono- and divalent ion transport (6, 7). Emerging subnanoporous membranes achieve selective monovalent ion separation and divalent ion exclusion via the pore-size sieving effect, where monovalent ions are partially dehydrated to facilitate the transport (8–10). Heretofore, whether a complete ion dehydration can contribute to the further promotion of ion transport has not been systematically explored.

Crown ethers are a class of cyclic ethylene oxide molecules with cavities of ~3 Å, similar to the sizes of bare monovalent ions including K^+, Na^+, and Li^+ (11–18), which have the potential to render ion transport in a complete dehydration form however not yet implemented. For example, crown ethers such as 18-crown-6 and 15-crown-5 derivatives have been assembled into lipid bilayers to construct ion channels for the transport of K^+ (19–22). Then, crown ethers are grafted onto polymers (23–26) or embedded within graphene membranes (27, 28) via the side-chain post-modification strategy. Such methods cannot guarantee sufficient crown ethers fixed in the channel due to the flexible side chains, and ions tend to transport in a hydration or partial dehydration form, circumventing the cavities of crown ethers.

Metal-organic frameworks (MOFs) are a class of porous materials constructed by metal ions or clusters coordinated with organic ligands, forming a window-cavity structure, where the sub-1-nm windows can sieve ions according to their sizes and the nanometer cavities can offer confined space to immobilize crown ethers for interaction screening of ions (29–31). Specifically, the chemical interactions can compensate for the energy penalty of ion dehydration, and the greater dehydration of ions exposes the ion's chemistry and, in turn, strengthens the interactions (32). For instance, 18-crown-6 ether (18C6) was encapsulated in the cavity of zeolite-imidazolate framework (ZIF), e.g., ZIF-67/ZIF-8, for selective monovalent ion transport, while the molecular size of 18C6 (5.7 Å) is much smaller than that of the ZIF cavity (11.6 Å) (33). As a result, the mismatch between 18C6 and the cavity generates gaps for hydrated ion transport, diminishing the interaction screening of crown ethers for monovalent ions. UiO-66, a well-known MOF for its hydrolytic stability (29), has been widely investigated for nanofluidic devices, desalination, and ion separation (34–36). Single-ion channels have been fabricated on the basis of UiO-66 derivative MOFs, showing enhanced monovalent ion transport probably due to the partial dehydration of ions (37, 38). UiO-66 membranes are generally prepared by the solvothermal reaction at a high temperature, and cracks between grain boundaries are prone to form during the cooling process, resulting in a declined ion selectivity (39, 40). Thus, the synthesis of UiO-66 membrane at a mild condition is highly demanded for the fabrication of crack-free MOF membranes and the intact confinement of size-matched crown ethers as well.

Herein, we report the in situ growth of UiO-66 confined crown ether (CE@UiO-66) membranes at a mild condition (Fig. 1A). The UiO-66 cavity of ~12 to 15 Å can perfectly confine the selected dibenzo-15-crown-5 (DB15C5) or dibenzo-18-crown-6 (DB18C6) with molecular sizes around 12 Å, and the UiO-66 window of ~8 Å can prevent the CEs from escaping (Fig. 1B). Compared to the pristine UiO-66 membrane, CE@UiO-66 membranes show enhanced monovalent ion diffusion coefficients and selectivities. In the binary-ion system, the monovalent cation permeation rates (e.g., K^+) and mono-/divalent cation selectivities (e.g., K^+/Mg^{2+}) vary from 0.9 to 1.2 mol m² hour⁻¹ and from 30 to 60 by the confinement of DB15C5 and DB18C6, respectively. First-principle calculations and molecular dynamic (MD) simulations reveal that monovalent ions are completely dehydrated

[1]Key Laboratory of Precision and Intelligent Chemistry, Department of Applied Chemistry, School of Chemistry and Materials Science, University of Science and Technology of China, Hefei 230026, China. [2]School of Chemistry and Chemical Engineering, Key Laboratory of Environment-Friendly Polymeric Materials of Anhui Province, Anhui University, Hefei 230601, China. [3]Hefei National Research Center for Physical Sciences at the Microscale, University of Science and Technology of China, Hefei 230026, China. [4]Department of Chemical and Biological Engineering, Monash University, Clayton, VIC 3800, Australia.
*Corresponding author. Email: xingyali@ustc.edu.cn (X.L.); twxu@ustc.edu.cn (T.X.)
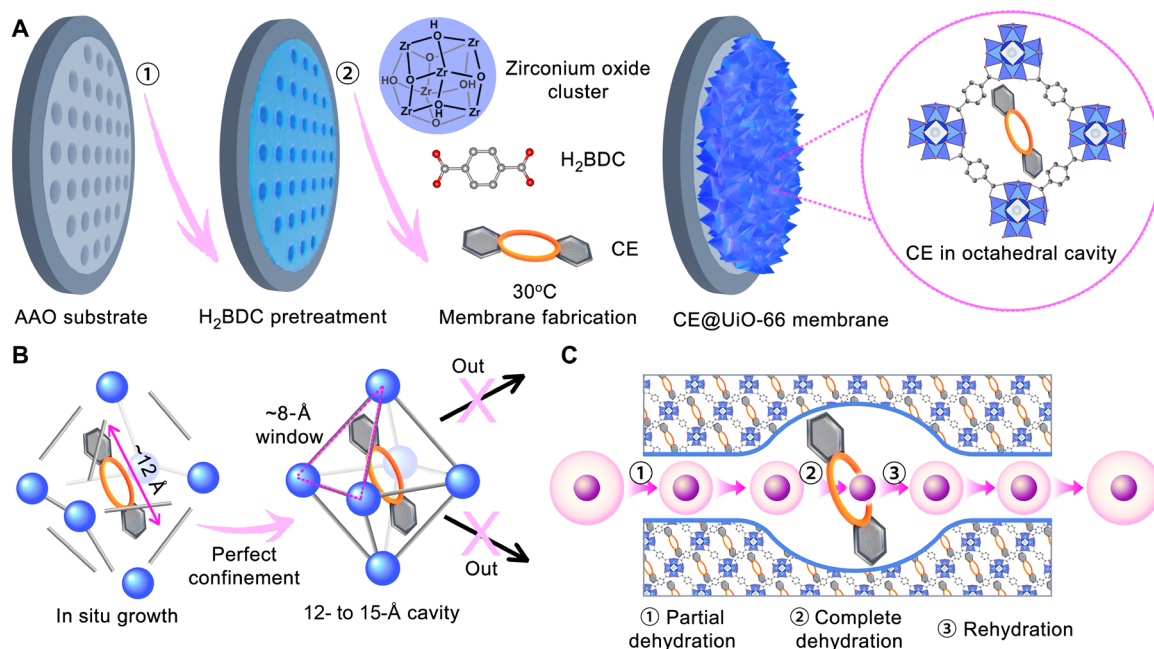†These authors contributed equally to this work.

Fig. 1. Fabrication of CE@UiO-66 membranes for fast monovalent ion transport. (A) Scheme of the fabrication of CE@UiO-66 membranes via the in situ growth at a mild condition (30°C). **(B)** Perfect confinement of CE (~12 Å) in the UiO-66 cavity. **(C)** Size and interaction sieving of monovalent ions in CE@UiO-66 membranes, where monovalent ions undergo a complete dehydration.

while transporting through the DB18C6@UiO-66 cavity (Fig. 1C) with lower energy barriers following the order of $K^+ < Na^+ < Li^+ < Mg^{2+}$ and higher transport rates of $K^+ > Na^+ > Li^+ > Mg^{2+}$ than through the UiO-66 cavity.

RESULTS

Fabrication of UiO-66 and CE@UiO-66 membranes at a mild condition

UiO-66, DB15C5@UiO-66, and DB18C6@UiO-66 membranes were fabricated on anodic alumina oxide (AAO) substrates via the in situ confinement and growth method, which was carried out in a self-designed Teflon holder. AAO discs with a pore size of 90 ± 10 nm and a diameter of 25 mm were used as the substrate. Before the preparation of CE@UiO-66 membranes, AAO substrates were pretreated with terephthalic acid (H_2BDC) at 130°C for 2 hours (Fig. 1A, step 1) to form a seeding layer for the growth of MOF membranes. After the temperature cooled to room temperature, the seeded AAO substrates were mounted in the Teflon holder, followed by the addition of zirconium oxide cluster (see Materials and Methods for the synthesis details), H_2BDC, and crown ethers (DB15C5 or DB18C6) as shown in Fig. 1A (step 2). A continuous DB15C5@UiO-66 or DB18C6@UiO-66 layer formed on the AAO substrate after 24 hours at 30°C. The synthesized UiO-66 crystals contain triangular windows of ~8 Å and octahedral cavities of ~12 to 15 Å (fig. S1). The molecular sizes of DB18C6 and DB15C5 are well matched with the octahedral cavity, endowing the perfect confinement of single CE in the cavity. After being incorporated in the UiO-66 cavity, DB18C6 and DB18C5 are unlikely to escape due to the end-capping by the smaller MOF window (Fig. 1B and fig. S2).

After the in situ confinement and growth, highly crystalline and continuous UiO-66, DB18C6@UiO-66, and DB15C5@UiO-66 membranes were successfully fabricated on the surface of AAO substrates. Scanning electron microscopy (SEM) images of the surface and cross section of UiO-66, DB15C5@UiO-66, and DB18C6@UiO-66 membranes are shown in Fig. 2 (A to F). The SEM images confirm the complete coverage of the AAO surface with UiO-66, DB15C5@UiO-66, and DB18C6@UiO-66 layers without any visible boundary defects and cracks. The membrane surface morphologies indicate the well intergrowth among UiO-66 crystals during the membrane formation process. The membrane cross-sectional images and energy-dispersive spectrometry mappings (Fig. 2G and fig. S3) show a uniform and continuous MOF layer attached tightly to the AAO substrate with a thickness of around 1 μm. X-ray diffraction (XRD) patterns of UiO-66, DB15C5@UiO-66, and DB18C6@UiO-66 crystals and membranes are the same as the simulated one, verifying the successful preparation of UiO-66 crystals and the high crystallinity of the membranes (Fig. 2H and fig. S4) (*29*). The XRD patterns also indicate that the incorporation of DB15C5 or DB18C6 during UiO-66 crystallization has no influence on the MOF structure. X-ray photoelectron spectroscopy spectra of UiO-66, DB15C5@UiO-66, and DB18C6@UiO-66 crystals and membranes also confirm the chemical structure of the MOF (fig. S5). The thermogravimetric analysis results of UiO-66, DB15C5@UiO-66, and DB18C6@UiO-66 crystals indicate a higher weight loss of CE@UiO-66 than that of UiO-66, signifying the existence of DB15C5/DB18C6 in UiO-66 cavity (Fig. 2I). The molar percentage of DB15C5 and DB18C6 molecules to the UiO-66 unit cells of DB15C5@UiO-66 and DB18C6@UiO-66 crystals is ~29.78 and 31.61%, respectively (see the Supplementary Materials for the calculation details). The Brunauer-Emmett-Teller surface area of DB15C5@UiO-66 and DB18C6@UiO-66 crystals calculated from the N_2 adsorption/desorption isotherm profiles is 732 and 751 $m^2 g^{-1}$, respectively, lower than that of UiO-66 crystals of 1135 $m^2 g^{-1}$ (fig. S6A). The
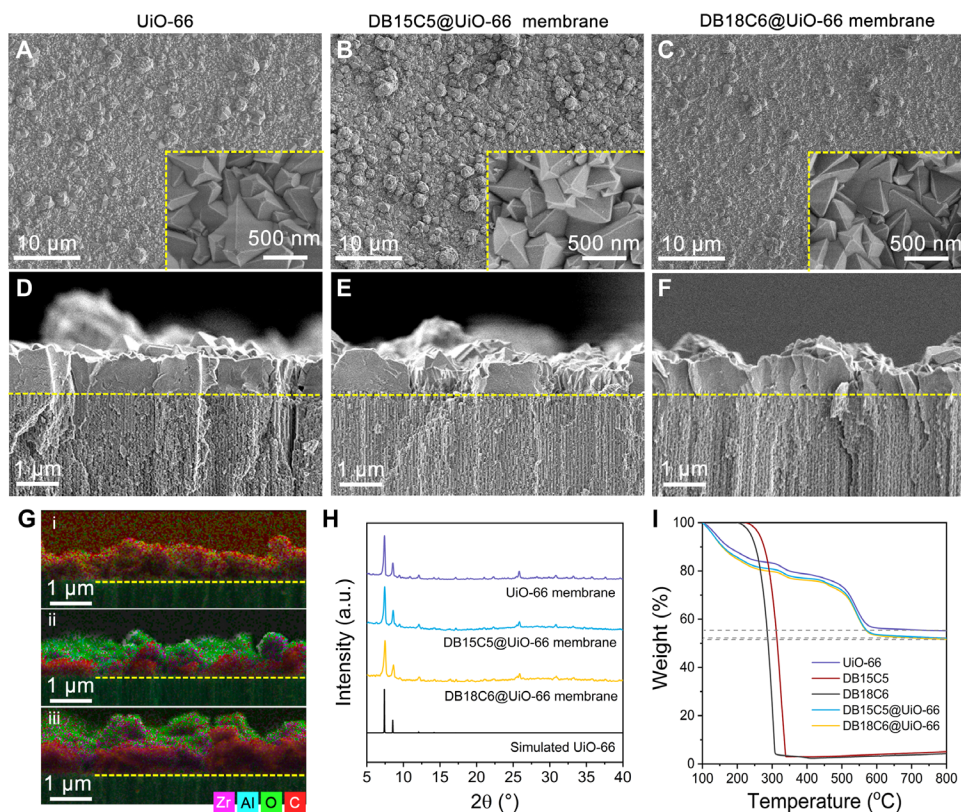
Fig. 2. Characterization of UiO-66, DB15C5@UiO-66, and DB18C6@UiO-66 membranes. Scanning electron microscopy (SEM) images of the surface of (**A**) UiO-66 membrane, (**B**) DB15C5@UiO-66 membrane, and (**C**) DB18C6@UiO-66 at low magnification; the insets are high-magnification images. SEM cross-sectional images of (**D**) UiO-66 membrane, (**E**) DB15C5@UiO-66 membrane, and (**F**) DB18C6@UiO-66 membrane. (**G**) Energy-dispersive spectrometry mapping of UiO-66 (i), DB15C5@UiO-66 (ii), and DB18C6@UiO-66 membranes (iii). (**H**) XRD patterns of UiO-66, DB15C5@UiO-66, and DB18C6@UiO-66 membranes. a.u., arbitrary units. (**I**) Thermogravimetric analysis of DB15C5, DB18C6, UiO-66, DB15C5@UiO-66, and DB18C6@UiO-66.

pore-size distributions show that the as-prepared UiO-66 and CE@UiO-66 at the mild-condition have a window of ~8 Å and a cavity of ~12 to 15 Å due to the lattice defects generated at a low temperature (fig. S6B and tables S1 and S2). In addition, the pore-size distributions of crown ether@UiO-66 display a decreased cavity size as compared to the pristine UiO-66 (fig. S6B), indicating that the DB15C5/DB18C6 molecules are trapped inside the UiO-66 cavities during the MOF formation and crystallization process.

Furthermore, the stability of UiO-66, DB15C5@UiO-66, and DB18C6@UiO-66 membranes in salt solutions (0.1 M KCl, 0.1 M NaCl, 0.1 M LiCl, and 0.1 M MgCl$_2$) was studied. The membrane XRD patterns show that their crystal structures remain unchanged after the 7-day treatment in the salt solutions (fig. S7). Thus, the as-prepared UiO-66, DB15C5@UiO-66, and DB18C6@UiO-66 membranes are used to study the ion transport properties and separation performance.

Ion transport properties in UiO-66 and CE@UiO-66 membranes

The ion transport properties in UiO-66 and CE@UiO-66 membranes were investigated under the concentration-driven diffusion (see the Supplementary Materials for the testing apparatus, fig. S8, and table S3). Aqueous solutions including 0.1 M LiCl, NaCl, KCl, and MgCl$_2$ are used as the feed solution in the single-ion system, and 0.1 M

KCl/0.1 M MgCl$_2$, 0.1 M NaCl/0.1 M MgCl$_2$, and 0.1 M LiCl/0.1 M MgCl$_2$ are used as feed solution in the binary-ion system, while the permeate side is deionized (DI) water. The concentration of various ions in the permeate solution was detected by inductively coupled plasma optical emission spectrometry.

As for the UiO-66 and CE@UiO-66 membranes, the K$^+$ and Na$^+$ ion permeation rates of DB18C6@UiO-66 membranes are obviously higher than those of the DB15C5@UiO-66 membranes, which are higher than those of the UiO-66 membranes, while the three membranes show similar Li$^+$ ion permeation rates (Fig. 3A). As expected, the Mg^{2+} ion permeation rates of UiO-66 membranes are higher than those of CE@UiO-66 membranes. The ion permeation rates of the three membranes follow the sequence of K$^+$ > Na$^+$ > Li$^+$ >> Mg^{2+} (Fig. 3A). The ion transport energy barrier is positively related to the ion diffusion coefficient, which is calculated to reflect the transport energy barrier of monovalent ions in the CE@UiO-66 membranes (Fig. 3B and table S4). The monovalent ion diffusion coefficients of the studied membranes (41–43) follow the order of DB18C6@UiO-66 > DB15C5@UiO-66 > UiO-66, indicating that the ion transport energy barrier complies with the opposite sequence. Considering that a strong interaction could compensate for an otherwise large energy barrier, DB18C6 has a stronger interaction with the monovalent ions than DB15C5, which are both stronger than those of the UiO-66. The diffusion coefficient of Mg^{2+} of the studied membranes follow the order of
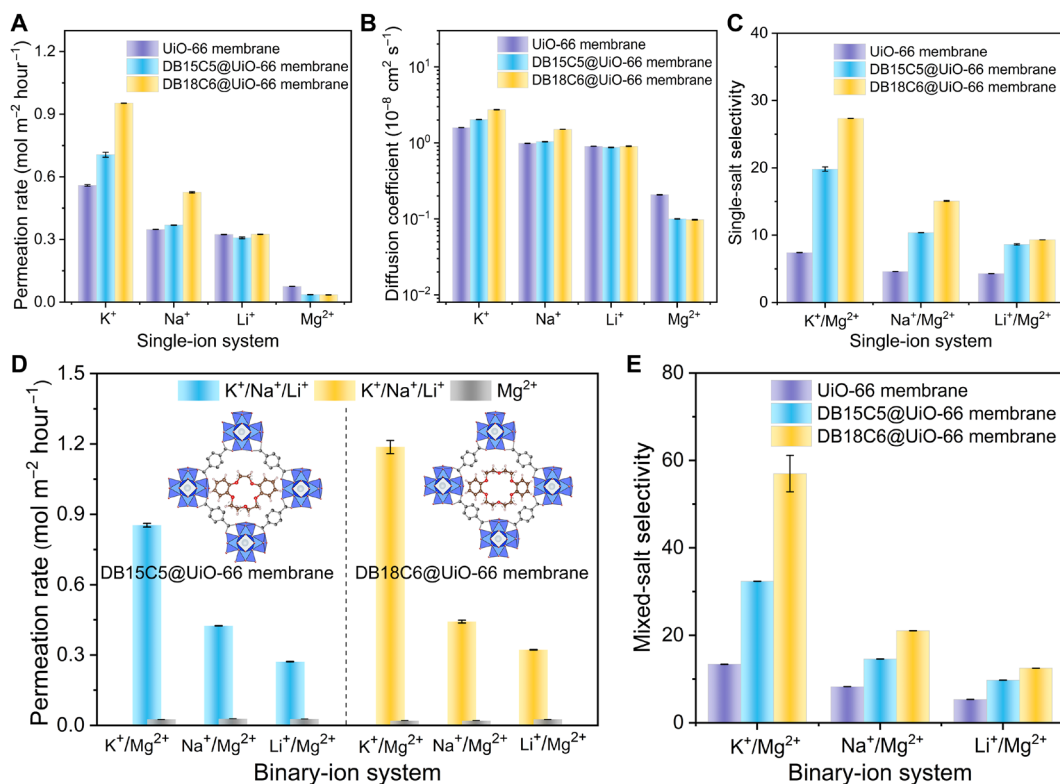
Fig. 3. Ion transport properties of UiO-66, DB15C5@UiO-66, and DB18C6@UiO-66 membranes. (**A**) Ion permeation rates of K^+, Na^+, Li^+, and Mg^{2+} of UiO-66, DB15C5@UiO-66, and DB18C6@UiO-66 membranes (single-ion system: 0.1 M KCl, 0.1 M NaCl, 0.1 M LiCl, and 0.1 M MgCl$_2$). (**B**) The calculated ion diffusion coefficients of UiO-66, DB15C5@UiO-66, and DB18C6@UiO-66 membranes. (**C**) Single-salt selectivities of UiO-66, DB15C5@UiO-66, and DB18C6@UiO-66 membranes calculated from single-ion permeation rates. (**D**) Permeation rates of DB15C5@UiO-66 and DB18C6@UiO-66 membranes in the binary-ion system. (**E**) Mixed-salt selectivities of UiO-66, DB15C5@UiO-66, and DB18C6@UiO-66 membranes in the binary-ion system.

DB18C6@UiO-66 < DB15C5@UiO-66 < UiO-66, suggesting that the transport of Mg^{2+} through the channels is dominated by the size sieving effect. CE@UiO-66 membranes exhibit much higher single-salt selectivities (calculated on the basis of the ion permeation rate of single-ion system) of monovalent ion (e.g., K^+/Mg^{2+}, Na^+/Mg^{2+}, and Li^+/Mg^{2+}) than those of UiO-66 membranes and the AAO substrate (Fig. 3C and figs. S9 and S10), which is enabled by the combination of the size sieving and interaction screening effects from the perfect confinement of CE in UiO-66. Moreover, the single-salt selectivities of DB18C6@UiO-66 membrane (i.e., K^+/Mg^{2+} of 27, Na^+/Mg^{2+} of 15, and Li^+/Mg^{2+} of 9.3) are higher than those of the DB15C5@UiO-66 membrane (i.e., K^+/Mg^{2+} of 20, Na^+/Mg^{2+} of 10, and Li^+/Mg^{2+} of 8.6). The reproduced ion permeation rates and selectivities in the single-ion system of UiO-66, DB15C5@UiO-66, and DB18C6@UiO-66 membranes are shown in fig. S10. In the binary-ion system, the permeation rates of monovalent cations remain similar to those of the single-ion system, while the permeation rate of Mg^{2+} decreases significantly (Fig. 3D), with the effect that the mixed-salt selectivities are substantially higher than the single-salt selectivities (Fig. 3E). Specifically, the K^+/Mg^{2+} selectivity of DB18C6@UiO-66 and DB15C5@UiO-66 membrane increases from 27 to 57 and from 20 to 32, respectively. As a comparison, there is no obvious increase in the mixed-salt mono-/divalent ion selectivity of UiO-66 membrane (i.e., K^+/Mg^{2+} of 13, Na^+/Mg^{2+} of 8.3, and Li^+/Mg^{2+} of 5.4). This finding can further confirm that the confined crown ethers have interaction screening

effects on monovalent ions rather than the divalent ion. Therefore, the CE@UiO-66 channels can facilitate the transport of monovalent ions while blocking the divalent ion when the monovalent ion is coexisted with the divalent ion, leading to an elevated mono-/divalent ion selectivity. Similar to the single-salt selectivity, the membrane mixed-salt selectivity follows the sequence of DB18C6@UiO-66 > DB15C5@UiO-66 > UiO-66. The reproduced permeation rates of UiO-66, DB15C5@UiO-66, and DB18C6@UiO-66 membranes in the binary-ion system are shown in figs. S11, S12, and S13, respectively. The results of selectivities in binary-component solution for repeatability test of UiO-66, DB15C5@UiO-66, and DB18C6@UiO-66 membranes are shown in fig. S14. Compared to other reported membranes under the concentration-driven gradient (figs. S15 and S16 and table S5), CE@UiO-66 membranes show an excellent ion permeation rate with a competitive selectivity.

Effect of concentration gradient on ion separation of DB18C6@UiO-66 membranes

To evaluate the effect of driving force for ion diffusion, different concentration gradients including 0.01, 0.05, 0.1, and 0.5 M are used for ion transport. Taking the DB18C6@UiO-66 membrane as an example, the ion permeation rates show a proportional rise to the concentration gradient (Fig. 4, A and B). Particularly, the K^+ permeation rate reaches 4.5 mol m^{-2} hour^{-1} as the concentration gradient increases to 0.5 M. Therefore, the single-salt selectivities in the single-ion system

remains quite similar (e.g., K^+/Mg^{2+} around 27, Na^+/Mg^{2+} around 15, and Li^+/Mg^{2+} around 10) even with varied concentration gradients from 0.01 to 0.5 M.

Stability of DB18C6@UiO-66 membranes for ion separation

The repetitive stability of the DB18C6@UiO-66 membrane for ion separation was evaluated by repeating the measurement five times both in the single- and binary-ion systems (Fig. 4, C and D). For the single-ion system, the K^+ permeation rates of UiO-66 and DB18C6@UiO-66 membranes display slight variations during the five consecutive tests, and the K^+/Mg^{2+} selectivities remain a stable range of 6 to 8 (fig. S17) and 22 to 26 (Fig. 4C and fig. S18), respectively. As for the binary-ion system, the K^+ permeation rates of DB18C6@UiO-66 membrane vary around 1.0 mol m^{-2} hour^{-1}, while the Mg^{2+} permeation rates stay around 0.015 mol m^{-2} hour^{-1}, resulting in a fluctuation of K^+/Mg^{2+} selectivity from 45 to 75. To verify the structural stability of the DB18C6@UiO-66 membrane after the repetitive stability test, the membrane crystallinity and morphology characterizations were performed. The DB18C6@UiO-66 membrane after testing five times remains a high crystallinity as revealed by the XRD pattern (fig. S19). The morphology of DB18C6@UiO-66 membrane after testing five times maintains an intact layer as confirmed by the SEM surface images (fig. S20). These results

demonstrate the excellent structural and operational stability of DB18C6@UiO-66 membranes.

Ion transport mechanism in DB18C6@UiO-66 channels

MD simulations are used to study the ion transport properties in UiO-66 and DB18C6@UiO-66 channels under the concentration-driven gradient. The diffusion coefficients using an Einstein relation were calculated by converting the slopes of the ion mean square displacement (MSD) versus time curves. In UiO-66 channels, the monovalent ion diffusion coefficients follow the order of $K^+ > Na^+ > Li^+$ (table S6), within the range from 1.47×10^{-5} to 2.39×10^{-5} cm^2 s^{-1}, where ions are partially dehydrated because of the size sieving of the UiO-66 window (Fig. 5A). In DB18C6@UiO-66 channels, the monovalent ion diffusion coefficients (table S6) range from 1.87×10^{-5} to 2.92×10^{-5} cm^2 s^{-1}, which are higher than those of the UiO-66 channels, and monovalent ion diffusion coefficients adhere to the same order of $K^+ > Na^+ > Li^+$ (Fig. 5B). After the confinement of DB18C6 in the UiO-66 cavity, the crown ether-ion interaction contributes to attracting monovalent ions and compensating for the dehydration energy barrier and thus facilitating them to transport through the cavity. The resultant ion diffusion coefficients from MD simulations follow the same sequence as that from the experimental ones.
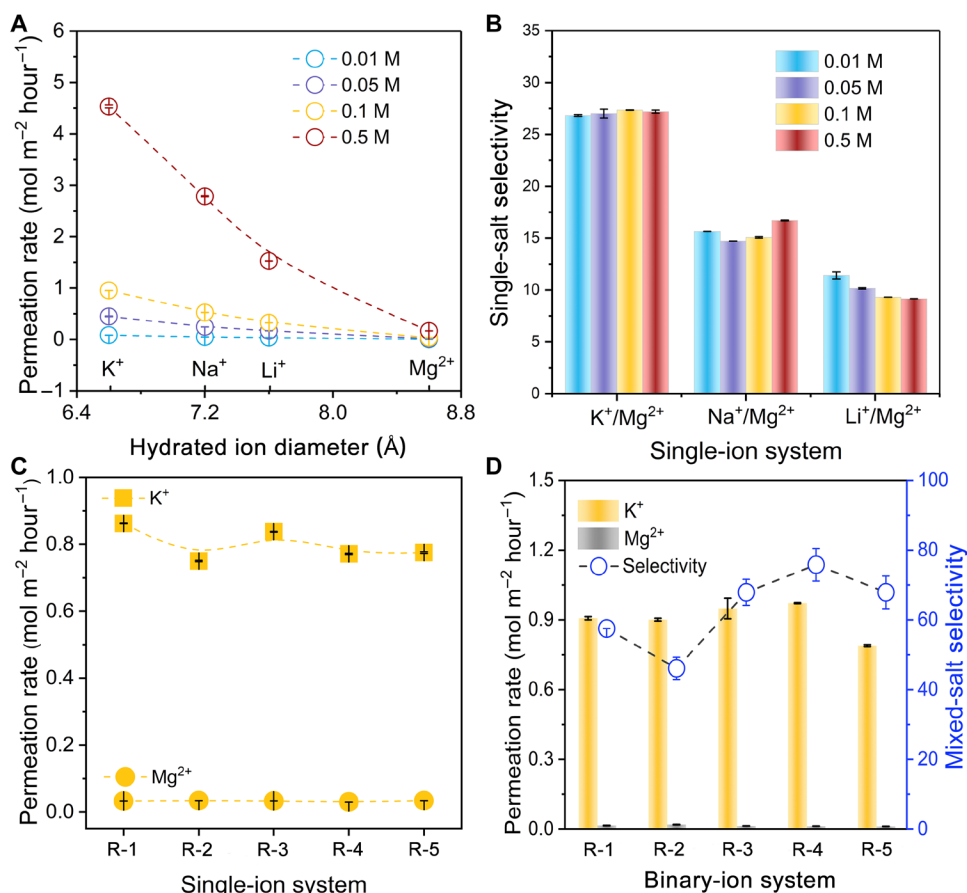

Fig. 4. The effect of concentration gradient on the ion separation performance and the repetitive stability of DB18C6@UiO-66 membranes. (**A**) Ion permeation rates of the DB18C6@UiO-66 membrane under different concentration gradients in the single-ion system (i.e., 0.01, 0.05, 0.1, and 0.5 M chloride salts). (**B**) Single-salt selectivities of the DB18C6@UiO-66 membrane under different concentration gradients. (**C**) Repetitive stability of DB18C6@UiO-66 membranes in the single-ion system (i.e., 0.1 M KCl and 0.1 M MgCl$_2$). (**D**) Repetitive stability of DB18C6@UiO-66 membranes in the binary-ion system (0.1 M KCl/0.1 M MgCl$_2$).
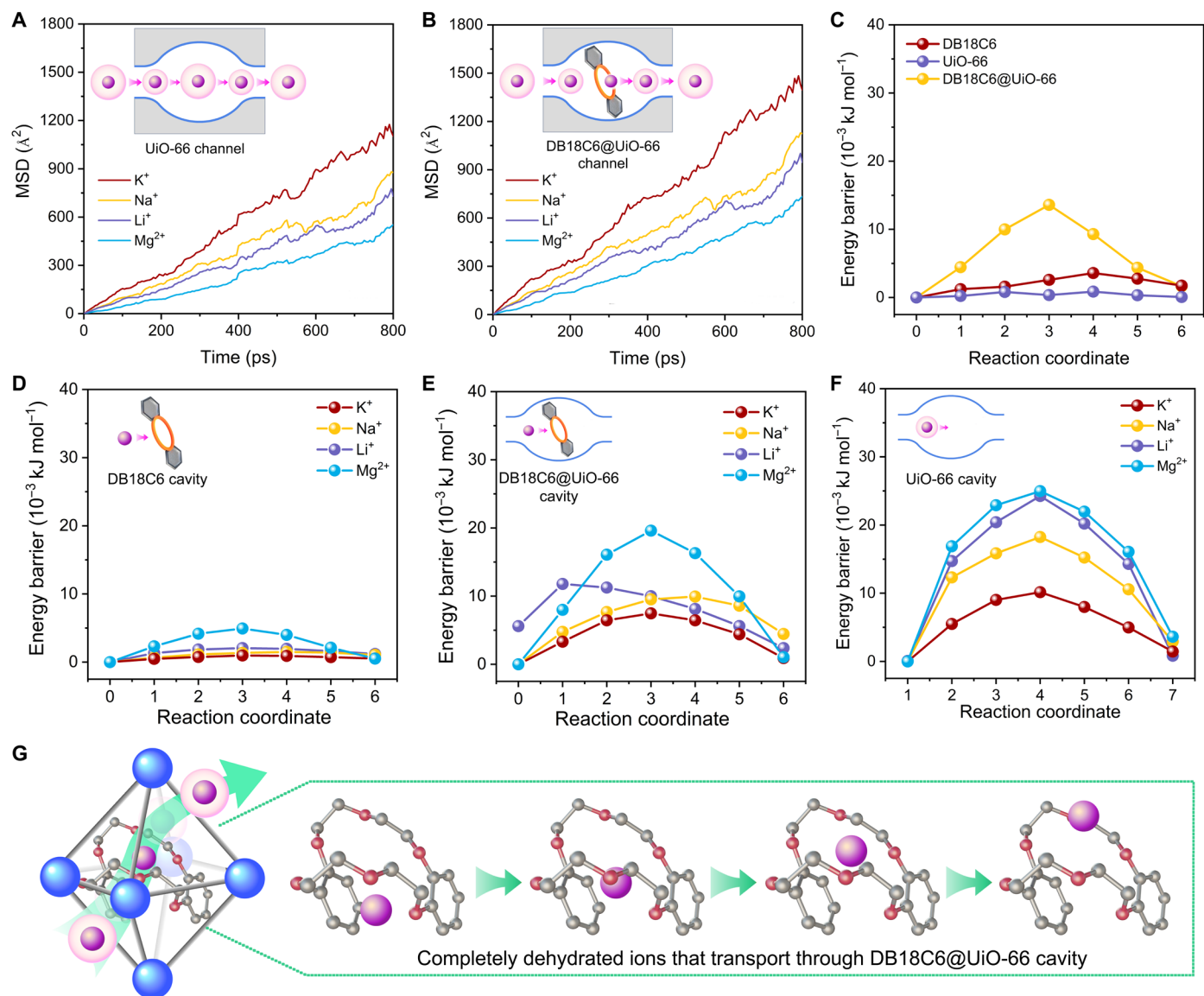
Fig. 5. Ion transport mechanism in DB18C6@UiO-66 channels. Mean square displacement (MSD) of ions that transport through (**A**) UiO-66 and (**B**) DB18C6@UiO-66 along with time. (**C**) Energy barriers of water molecules that transport through the DB18C6, UiO-66, and DB18C6@UiO-66 cavities. Energy barriers of ions that transport through (**D**) DB18C6 cavity and (**E**) DB18C6@UiO-66 cavity. (**F**) Energy barriers of ions that transport through the UiO-66 cavity. (**G**) Simplified scheme of completely dehydrated ions that transport through the DB18C6@UiO-66 cavity.

To figure out how the ions transport through the DB18C6@UiO-66 cavity, the first-principle calculations are used. First, water molecules that transport through the DB18C6, UiO-66, and DB18C6@UiO-66 cavities are studied. The calculated rate of water passing through the cavity of DB18C6, UiO-66, and DB18C6@UiO-66 is 8.25×10^{6}, 2.83×10^{11}, and 6.14×10^{-10} molecules mol^{-1} s^{-1}, respectively, indicating that nearly no water molecules can pass through the DB18C6@UiO-66 cavity. The water transport energy barriers through the above three cavities are shown in Fig. 5C, fig. S21, and table S7, where the energy barrier for water passing through the DB18C6@UiO-66 cavity is much higher than those of the DB18C6 and UiO-66 cavities. Additional water migration experiments were performed to investigate the water transport property in UiO-66 and DB18C6@UiO-66 membranes. The reduced water volume of

the feed solution of UiO-66 membrane is much higher than that of the DB18C6@UiO-66 membrane with a loading of 31.61% (fig. S22), confirming that the water molecules can hardly transport through DB18C6@UiO-66 cavities. The measured diameter of water is 3.34 Å in the calculations, which is larger than the studied bare ions' diameters but smaller than their hydrated diameters (table S8) (*44*). Consequently, ions should most likely be completely dehydrated (i.e., in the bare ion form) to transport through the DB18C6@UiO-66 cavity. As a comparison, the ions are partially dehydrated when passing through the DB18C6 and UiO-66 cavities, indicated by the results from the radial distribution functions (RDFs) for DB18C6 and UiO-66 (fig. S23). Then, we investigate the ion transport energy barriers in the DB18C6, DB18C6@UiO-66, and UiO-66 cavities. In the DB18C6 cavity, the energy barrier for ion transport

follows the order of $K^+ < Na^+ < Li^+ < Mg^{2+}$ (Fig. 5D and table S9), which is exerted by the interaction screening of the crown ether. This can reveal that the interaction between the crown ether and ions follows the order of $K^+ > Na^+ > Li^+ > Mg^{2+}$ (45, 46). By contrast, a higher energy barrier is required to overcome for ions passing through the DB18C6@UiO-66 cavity (Fig. 5E and table S10). The ion transport energy barrier through the DB18C6@UiO-66 cavity is lower than that of the UiO-66 cavity because the perfectly confined crown ether-ion interaction can compensate the energy loss of the ion dehydration (Fig. 5F and table S11). The enhanced monovalent ion transport rates of DB18C6@UiO-66 channels can be ascribed to the bare ions that transport through the DB18C6@UiO-66 cavities with lower energy barriers (Fig. 5G and fig. S24). In addition, the energy barrier difference between the monovalent ions and Mg^{2+} of the DB18C6@UiO-66 cavity is larger than that of the UiO-66 cavity, leading to a higher selectivity for K^+/Mg^{2+}, Na^+/Mg^{2+}, and Li^+/Mg^{2+} as observed in the experimental findings.

DISCUSSION

In summary, crack-free CE@UiO-66 membranes with well size-matched crown ethers in the cavity are constructed by the in situ growth at a mild condition. The resultant CE@UiO-66 membranes show enhanced monovalent ion permeation rate and selectivity compared to the pristine UiO-66 membranes, which can be attributed to the complete dehydration of monovalent ions arising from the combined size sieving and interaction screening effects. Theoretical simulations and calculations suggest that fully dehydrated ions can transport through the DB18C6@UiO-66 channel, leading to a fast transport of monovalent ions with a low energy barrier, as evidenced by the elevated ion diffusion coefficients observed in the experiment. The perfect confinement of crown ether strategy endows the integration of size sieving and interaction screening in one membrane and improves the ion permeability without sacrificing the ion selectivity, offering guidelines for the design and construction of highly efficient ion separation membranes.

MATERIALS AND METHODS

Materials

Zirconlum (IV) propoxide solution [$Zr(OnPr)_4$, 70.0 wt % in 1-propanol] was purchased from Aladdin (Shanghai, China). Terephthalic acid (H_2BDC; 99.0%) was purchased from TCI (Shanghai, China) development Co. Ltd. DB18C6 ether (98.0%) was obtained from Energy Chemical (Anhui, China). DB15C5 ether (95%) was received from Yongguang Chemical (Hubei, China). N,N-dimethylformamide (DMF); acetic acid (CH_3COOH; 99.5%); 1-propanol (99.5%), triethylamine (98.0%); ethanol (C_2H_5OH; 99.7%); and analytical grade KCl, NaCl, LiCl, and $MgCl_2$ were obtained from China National Pharmaceutical Group Industry Co. Ltd. (Beijing, China). All reagents and solvents were used as received, without further purification. DI water was used throughout the experiments. AAO (Hefei Pu-Yuan Nano Technology Ltd.) discs were used as substrates.

Synthesis of UiO-66 powders

The UiO-66 powders were fabricated following the procedures in previous work (47).

Step (1) SBU intermediate preparation: A total of 497 μl of 70% $Zr(OnPr)_4$ solution, 0.36 g of 1-propanol, 50 ml of DMF, and 28 ml of acetic acid were added to a 100-ml Teflon vial. The colorless solution was heated in an oven at 130°C for 2 hours until a yellow solution was observed. Then, the solution gradually cooled to room temperature.

Step (2) UiO-66 powder preparation: H_2BDC (0.53 g) was added to the solution from step (1). The solution was briefly sonicated for 30 s. After that, the mixture was stirred and reacted at 30°C for 24 hours. UiO-66 powders were separated by centrifugation and then washed with DMF and acetone at least three times until they have been thoroughly washed. The obtained powders were dried at 80°C for 12 hours.

Synthesis of DB15C5@UiO-66/DB18C6@UiO-66 powders

To obtain the DB15C5@UiO-66/DB18C6@UiO-66 powders, the procedure is the same as the synthesis of UiO-66 powders, except for the addition of DB15C5/DB18C6 in step (2). Briefly, in step (2), H_2BDC (0.53 g) and DB15C5 (1.0 g)/DB18C6 (1.1 g) were added to the solution obtained from step (1). Note that, all the powders were thoroughly washed and used for the following experiments (figs. S25 to S27).

Synthesis of UiO-66 membranes

Step (1) SBU intermediate preparation: The same procedure was followed as step (1) of synthesis of UiO-66 powders.

Step (2) Pretreatment: Simultaneously with step (1), AAO substrates (pore size of 90 ± 10 nm and diameter of 25 mm) were pretreated with H_2BDC. Briefly, H_2BDC (0.53 g) and 15 ml of DMF were add to a vial. The solution was sonicated until H_2BDC dissolved. Then, an AAO substrate was immersed into the solution for pretreatment at 130°C for 2 hours.

Step (3) UiO-66 membrane preparation: The AAO substrate was taken out from H_2BDC solution in step (2) and then mounted on a homemade Teflon device. H_2BDC (0.53 g) was added to the solution from step (1). The whole device was immersed in the solution. After 24 hours, the membrane was taken out and washed with DMF three times. The membrane was immersed in DMF for 12 hours and then stored in ethanol before test.

Preparation of DB15C5@UiO-66/DB18C6@UiO-66 membranes

The preparation procedure of DB15C5@UiO-66/DB18C6@UiO-66 membranes is the same as the UiO-66 membrane, except for the addition of DB15C5/DB18C6 in step (3). Briefly, in step (3), H_2BDC (0.53 g) and DB15C5 (1.0 g)/DB18C6 (1.1 g) were added to the solution obtained from step (1).

Ion separation performance under the concentration-driven gradient

The experiments of ion separation performance were tested under the concentration-driven gradient. A homemade apparatus with feed and permeate chambers was separated by mounting the membrane between the two chambers (fig. S8). Notably, the MOF layer side faces the feed chamber.

For the single-ion system, 0.1 M electrolyte solutions (KCl, NaCl, LiCl, and $MgCl_2$) were separately added to the feed chamber, while DI water was added to the permeate chamber as the initial solution. Two chambers were kept stirring during the experiment. After each test, the samples were drawn from the permeate chamber. DI water was used to wash the test apparatus for at least 10 min. The inductively

coupled plasma optical emission spectrometer (ICAP 7400, Thermo Fisher Scientific, USA) was used to measure the concentration of ions. The ion permeation rate of the membranes was calculated by the ion concentration change in the permeate chamber.

Ion permeation rate ($J_{Nn}{}^+$; mol per square meter per hour) can be calculated by

$$J_{N^{n+}} = \frac{(C_t - C_0) \cdot V}{A_m \cdot t} \quad (1)$$

where C_0 and C_t represent the ions' (N^{n+}) molar concentrations in the permeate chamber before ($t = 0$ hours) and after ($t = 0.5$ hours) the test, respectively. V is the solution volume in the test chamber, which is 1.5×10^{-2} liters in this work. The membrane effective surface area (1.13×10^{-4} m^2) is denoted as A_m.

The membrane single-salt selectivity s can be described as

$$S_{M^+/D^{2+}} = \frac{J_{M^+}}{J_{D^{2+}}} \quad (2)$$

where $J_M{}^+$ and $J_D{}^{2+}$ (mol per square meter per hour) represent the permeation rates of monovalent and divalent cations after the experiment, respectively.

The same test procedure as the single-ion system was executed for the binary-ion system, except for the binary electrolyte solutions, such as 0.1 M KCl/ 0.1 M MgCl$_2$, 0.1 M NaCl/0.1 M MgCl$_2$, or 0.1 M LiCl/ 0.1 M MgCl$_2$, which were separately used in the feed chamber.

For the study of ion transport properties under different concentration-driven gradients, the same test procedure was applied, except for the different concentration of the electrolyte solutions (0.01, 0.05, 0.1, and 0.5 M KCl and MgCl$_2$) were used in the feed chamber.

The diffusion coefficients (Fig. 3B and table S4) of ions in UiO-66, DB15C5@UiO-66, and DB18C6@UiO-66 membranes were calculated with the following equation

$$D = \frac{P_s}{K_s} \quad (3)$$

where the diffusion coefficient of ions in the membrane is denoted as D. $\langle P_s \rangle$ is the average salt permeability coefficient. K_s is the partition coefficient. In this study, the membrane is composed of a crystalline layer based on an inorganic substrate, thus $K_s = 1$.

The average salt permeability coefficients were calculated from

$$D = \langle P_s \rangle = -\ln\left[1 - \frac{2(C_s^s)_L[t]}{(C_s^s)_0[0]} \right] \cdot \frac{VL}{2A_m t} \quad (4)$$

where $2(C_s^s)_L[t]$ is the molar salt concentration in the downstream solution at time t (1800 s), $(C_s^s)_0[0]$ is the initial salt concentration in the upstream chamber, A_m is the geometric area available for mass transfer (1.13 cm^2), and V is the volume of the upstream and downstream solutions (15 ml).

The repetitive stability of ion separation performance

The same test procedure as in the single-ion system and the binary-ion system was performed for the repetitive stability of ion separation performance. For example, R-2 represents the result of the second repetitive stability test. We repeated five times to check the reproducibility of the ion separation performance.

Water migration experiments

The same apparatus of ion separation performance test was used to test water migration of UiO-66 and DB18C6@UiO-66 membranes. The feed solution (15 ml, DI water) and draw solution (15 ml, 1.0 M NaCl) were separated by the membrane, and the volume of two chambers was measured after 12 hours (fig. S22).

MD simulations

MD simulations were carried out to simulate the transport of ions in MOF channels and crown ether cavities by using the GROMACS (2020.4) and the open-source molecular simulation software LAMMPS (47). For the simulation of ion transport, the model system (fig. S28) is similar to that of the experiment (fig. S8). All the simulations were conducted under the NVT (constant number of particles, volume, and temperature). The NVT ensemble at 300 K and the Nosé-Hoover thermostat method were applied to control these MD calculations (48, 49). Herein, the time step was set to 1 fs, and the total time duration was 5 ns. The COMPASS force field was applied to describe the interaction between the intra- and intermolecules. The contribution of long-range interactions were calculated via the particle-particle-particle-mesh solver (50). The cutoff distance for the Lennard-Jones and Coulombic interaction was set to 12 Å. The RDF for DB18C6 and UiO-66 was calculated to evaluate the hydration state of ions (fig. S23).

MSD analysis was used to determine the mode of displacement of ions over time. From the temperature-versus-time curve and the total energy–versus–time curve, the simulation system came into a steady state (fig. S29). In the "Ion transport mechanism in DB18C6@UiO-66 channels" section, the MSD profiles from the initial point to 1000 ps were shown as a representative.

In addition, MSD analysis can be used to calculate the parameters of ion movement, namely, the ion diffusion coefficient. The ion diffusion coefficients (D_E) of UiO-66 and DB18C6@UiO-66 membranes were calculated by converting the slopes (k) of the MSD-versus-time curves via an Einstein relation as the following equation

$$D_E = \frac{1}{6} \cdot k \quad (5)$$

where number 6 represents the direction of atomic diffusion. Note that the slope for calculating the diffusion coefficient is taken from the linear portion of the MSD-versus-time curve.

First-principle calculations

First-principle calculations were implemented in the Vienna Ab initio Simulation Package (VASP) to simulate the diffusion ability of Li$^+$, Na$^+$, K$^+$, and Mg^{2+} ions in the DB18C6 and DB18C6@UiO-66 cavities (51, 52). The generalized gradient approximation within the Perdew-Burke-Ernzerhof formalism was used to describe the exchange-correlation potential (53). The projector augmented wave method was applied to simulate the crown ether-ion interaction (54). A plane-wave cutoff energy of 500 eV was used in these calculations. In addition, the convergence threshold for the geometry optimizations was set to 10^{-5} eV in energy and 0.01 eV Å^{-1} in force. A gamma-point VASP was applied for all the calculations. In addition, the dispersion correction of D3 (55) was adopted for all the calculations in this work. The climbing image nudged elastic band (CI-NEB) method was taken to

search the minimum energy pathway for ion passing through the cavities of DB18C6, UiO-66, and DB18C6@UiO-66 (56, 57). Seven images were inserted for CI-NEB calculations with the initial and final positions included. The intermediate images were relaxed until the forces were smaller than 0.05 eV/Å, which can reduce the time consumption. The energy barriers of the Li^+, Na^+, K^+, and Mg^{2+} ions passing through the cavities were calculated by the following equation

$$E_{barrier} = E_{TS} - E_{stable} \qquad (6)$$

in which $E_{barrier}$ is the energy barrier of the system; E_{TS} and E_{stable} are the energy of the transition state and stable configuration of the ion diffusion in the cavity, respectively.

Supplementary Materials
This PDF file includes:
Supplementary Text
Figs. S1 to S29
Tables S1 to S11
References

REFERENCES AND NOTES

1. P. Srimuk, X. Su, J. Yoon, D. Aurbach, V. Presser, Charge-transfer materials for electrochemical water desalination, ion separation and the recovery of elements. *Nat. Rev. Mater.* **5**, 517–538 (2020).
2. M. Jian, R. Qiu, Y. Xia, J. Lu, Y. Chen, Q. Gu, R. Liu, C. Hu, J. Qu, H. Wang, X. Zhang, Ultrathin water-stable metal-organic framework membranes for ion separation. *Sci. Adv.* **6**, eaay3998 (2020).
3. Z. Zhu, D. Wang, Y. Tian, L. Jiang, Ion/molecule transportation in nanopores and nanochannels: From critical principles to diverse functions. *J. Am. Chem. Soc.* **141**, 8658–8669 (2019).
4. T. Xu, B. Wu, L. Hou, Y. Zhu, F. Sheng, Z. Zhao, Y. Dong, J. Liu, B. Ye, X. Li, L. Ge, H. Wang, T. Xu, Highly ion-permselective porous organic cage membranes with hierarchical channels. *J. Am. Chem. Soc.* **144**, 10220–10229 (2022).
5. T. Xu, Ion exchange membranes: State of their development and perspective. *J. Membr. Sci.* **263**, 1–29 (2005).
6. F. Sheng, L. Hou, X. Wang, M. Irfan, M. A. Shehzad, B. Wu, X. Ren, L. Ge, T. Xu, Electro-nanofiltration membranes with positively charged polyamide layer for cations separation. *J. Membr. Sci.* **594**, 117453 (2020).
7. N. White, M. Misovich, A. Yaroshchuk, M. L. Bruening, Coating of nafion membranes with polyelectrolyte multilayers to achieve high monovalent/divalent cation electrodialysis selectivities. *ACS Appl. Mater. Inter.* **7**, 6620–6628 (2015).
8. H. Zhang, J. Hou, Y. Hu, P. Wang, R. Ou, L. Jiang, J. Z. Liu, B. D. Freeman, A. J. Hill, H. Wang, Ultrafast selective transport of alkali metal ions in metal organic frameworks with subnanometer pores. *Sci. Adv.* **4**, eaaq0066 (2018).
9. Z.-Y. Jiang, H.-L. Liu, S. A. Ahmed, S. Hanif, S.-B. Ren, J.-J. Xu, H.-Y. Chen, X.-H. Xia, K. Wang, Insight into ion transfer through the sub-nanometer channels in zeolitic imidazolate frameworks. *Angew. Chem. Int. Ed.* **56**, 4767–4771 (2017).
10. X. Li, G. Jiang, M. Jian, C. Zhao, J. Hou, A. W. Thornton, X. Zhang, J. Z. Liu, B. D. Freeman, H. Wang, L. Jiang, H. Zhang, Construction of angstrom-scale ion channels with versatile pore configurations and sizes by metal-organic frameworks. *Nat. Commun.* **14**, 286 (2023).
11. C. J. Pedersen, Cyclic polyethers and their complexes with metal salts. *J. Am. Chem. Soc.* **89**, 7017–7036 (1967).
12. H. Zhang, R. Ye, Y. Mu, T. Li, H. Zeng, Small molecule-based highly active and selective K^+ transporters with potent anticancer activities. *Nano Lett.* **21**, 1384–1391 (2021).
13. J. Lu, G. Jiang, H. Zhang, B. Qian, H. Zhu, Q. Gu, Y. Yan, J. Z. Liu, B. D. Freeman, L. Jiang, H. Wang, An artificial sodium-selective subnanochannel. *Sci. Adv.* **9**, eabq1369 (2023).
14. A. Smolyanitsky, E. Paulechka, K. Kroenlein, Aqueous ion trapping and transport in graphene-embedded 18-crown-6 ether pores. *ACS Nano* **12**, 6677–6684 (2018).
15. N. Li, F. Chen, J. Shen, H. Zhang, T. Wang, R. Ye, T. Li, T. P. Loh, Y. Y. Yang, H. Zeng, Buckyball-based spherical display of crown ethers for *de novo* custom design of ion transport selectivity. *J. Am. Chem. Soc.* **142**, 21082–21090 (2020).
16. S. J. Warnock, R. Sujanani, E. S. Zofchak, S. Zhao, T. J. Dilenschneider, K. G. Hanson, S. Mukherjee, V. Ganesan, B. D. Freeman, M. M. Abu-Omar, Engineering Li/Na selectivity in 12-Crown-4–functionalized polymer membranes. *Proc. Natl. Acad. Sci. U.S.A.* **118**, e2022197118 (2021).
17. L. Jin, C. Sun, Z. Li, J. Shen, H. Zeng, A K^+-selective channel with a record-high K^+/Na^+ selectivity of 20.1. *Chem. Commun.* **59**, 3610–3613 (2023).
18. J. Li, Y. Shi, C. Qi, B. Zhang, X. Xing, Y. Li, T. Chen, X. Mao, Z. Zuo, X. Zhao, Z. Pan, L. Li, X. Yang, C. Li, Charging metal-organic framework membranes by Incorporating crown ethers to capture cations for ion sieving. *Angew. Chem. Int. Ed.* **62**, e202309918 (2023).
19. S. A. Hamidinia, G. E. Steinbaugh, W. L. Erdahl, R. W. Taylor, D. R. Pfeiffer, Selective transport of Pb^{2+} and Cd^{2+} across a phospholipid bilayer by a cyclohexanemonocarboxylic acid-capped 15-crown-5 ether. *J. Inorg. Biochem.* **100**, 403–412 (2006).
20. L. He, T. Zhang, C. Zhu, T. Yan, J. Liu, Crown ether-based ion transporters in bilayer membranes. *Chem. A Eur. J.* **29**, e202300044 (2023).
21. T. Yan, S. Liu, C. Li, J. Xu, S. Yu, T. Wang, H. Sun, J. Liu, Flexible single-chain-heteropolymer-derived transmembrane ion channels with high K^+ selectivity and tunable pH-gated characteristics. *Angew. Chem. Int. Ed.* **61**, e202210214 (2022).
22. C. Ren, J. Shen, H. Zeng, Combinatorial evolution of fast-conducting highly selective K^+-channels via modularly tunable directional assembly of crown ethers. *J. Am. Chem. Soc.* **139**, 12338–12341 (2017).
23. D. Sun, Y. Zhu, M. Meng, Y. Qiao, Y. Yan, C. Li, Fabrication of highly selective ion imprinted macroporous membranes with crown ether for targeted separation of lithium ion. *Sep. Purif. Technol.* **175**, 19–26 (2017).
24. P. Wang, J. Dai, Y. Ma, L. Chen, J. Pan, Fabrication and evaluation of aminoethyl benzo-12-crown-4 functionalized polymer brushes adsorbents formed by surface-initiated ATRP based on macroporous polyHIPEs and postsynthetic modification. *Chem. Eng. J.* **380**, 122495 (2020).
25. J. Li, H. Yi, M. Wang, F. Yan, Q. Zhu, S. Wang, J. Li, B. He, Z. Cui, Preparation of crown-ether-functionalized polysulfone membrane by in situ surface grafting for selective adsorption and separation of Li^+. *Chem. Sel.* **5**, 3321–3329 (2020).
26. Y. Wang, Z. Liu, F. Luo, H.-Y. Peng, S.-G. Zhang, R. Xie, X.-J. Ju, W. Wang, Y. Faraj, L.-Y. Chu, A novel smart membrane with ion-recognizable nanogels as gates on interconnected pores for simple and rapid detection of trace lead(II) ions in water. *J. Membr. Sci.* **575**, 28–37 (2019).
27. J.-Q. Hu, Z. Liu, K. Deng, Z.-H. Chen, Q.-W. Cai, Y. Faraj, R. Xie, X.-J. Ju, W. Wang, L.-Y. Chu, A novel membrane with ion-recognizable copolymers in graphene-based nanochannels for facilitated transport of potassium ions. *J. Membr. Sci.* **591**, 117345 (2019).
28. A. Fang, K. Kroenlein, D. Riccardi, A. Smolyanitsky, Highly mechanosensitive ion channels from graphene-embedded crown ethers. *Nat. Mater.* **18**, 76–81 (2019).
29. J. H. Cavka, S. Jakobsen, U. Olsbye, N. Guillou, C. Lamberti, S. Bordiga, K. P. Lillerud, A new zirconium inorganic building brick forming metal organic frameworks with exceptional stability. *J. Am. Chem. Soc.* **130**, 13850–13851 (2008).
30. Y. Liang, E. Li, K. Wang, Z.-J. Guan, H.-h. He, L. Zhang, H.-C. Zhou, F. Huang, Y. Fang, Organo-macrocycle-containing hierarchical metal–organic frameworks and cages: Design, structures, and applications. *Chem. Soc. Rev.* **51**, 8378–8405 (2022).
31. D. W. Lim, S. A. Chyun, M. P. Suh, Hydrogen storage in a potassium-ion-bound metal–organic framework incorporating crown ether struts as specific cation binding sites. *Angew. Chem. Int. Ed.* **126**, 7953–7956 (2014).
32. R. Epsztein, R. M. DuChanois, C. L. Ritt, A. Noy, M. Elimelech, Towards single-species selectivity of membranes with subnanometre pores. *Nat. Nanotechnol.* **15**, 426–436 (2020).
33. L. Ma, X. Han, S. Zhang, Z. Zeng, R. Song, X. Chen, D. Hou, L. Wang, Artificial monovalent metal ion-selective fluidic devices based on crown ether@ metal–organic frameworks with subnanochannels. *ACS Appl. Mater. Inter.* **14**, 13611–13621 (2022).
34. X. Li, Y. Liu, J. Wang, J. Gascon, J. Li, B. Van der Bruggen, Metal–organic frameworks based membranes for liquid separation. *Chem. Soc. Rev.* **46**, 7124–7144 (2017).
35. J. Hou, H. Wang, H. Zhang, Zirconium metal–organic framework materials for efficient ion adsorption and sieving. *Ind. Eng. Chem. Res.* **59**, 12907–12923 (2020).
36. H. Zhang, X. Li, J. Hou, L. Jiang, H. Wang, Angstrom-scale ion channels towards single-ion selectivity. *Chem. Soc. Rev.* **51**, 2224–2254 (2022).
37. J. Lu, H. Zhang, J. Hou, X. Li, X. Hu, Y. Hu, C. D. Easton, Q. Li, C. Sun, A. W. Thornton, M. R. Hill, X. Zhang, G. Jiang, J. Z. Liu, A. J. Hill, B. D. Freeman, L. Jiang, H. Wang, Efficient metal ion sieving in rectifying subnanochannels enabled by metal–organic frameworks. *Nat. Mater.* **19**, 767–774 (2020).
38. X. Li, H. Zhang, P. Wang, J. Hou, J. Lu, C. D. Easton, X. Zhang, M. R. Hill, A. W. Thornton, J. Z. Liu, B. D. Freeman, A. J. Hill, L. Jiang, H. Wang, Fast and selective fluoride ion conduction in sub-1-nanometer metal-organic framework channels. *Nat. Commun.* **10**, 2490 (2019).
39. A. L. Semrau, S. Wannapaiboon, S. P. Pujari, P. Vervoorts, B. Albada, H. Zuilhof, R. A. Fischer, Highly porous nanocrystalline UiO-66 thin films via coordination modulation controlled step-by-step liquid-phase growth. *Cryst. Growth Des.* **19**, 1738–1747 (2019).
40. S. Friebe, B. Geppert, F. Steinbach, J. Caro, Metal–organic framework UiO-66 layer: A highly oriented membrane with good selectivity and hydrogen permeance. *ACS Appl. Mater. Inter.* **9**, 12878–12885 (2017).

41. J. Kamcev, D. R. Paul, G. S. Manning, B. D. Freeman, Accounting for frame of reference and thermodynamic non-idealities when calculating salt diffusion coefficients in ion exchange membranes. *J. Membr. Sci.* **537**, 396–406 (2017).

42. J. Kamcev, D. R. Paul, B. D. Freeman, Ion activity coefficients in ion exchange polymers: Applicability of manning's counterion condensation theory. *Macromolecules* **48**, 8011–8024 (2015).

43. J. Kamcev, M. Galizia, F. M. Benedetti, E.-S. Jang, D. R. Paul, B. D. Freeman, G. S. Manning, Partitioning of mobile ions between ion exchange polymers and aqueous salt solutions: Importance of counter-ion condensation. *Phys. Chem. Chem.Phys.* **18**, 6021–6031 (2016).

44. C. W. Kammeyer, D. R. Whitman, Quantum mechanical calculation of molecular radii. I. Hydrides of elements of perodic groups IV through VII. *J. Chem. Phys.* **56**, 4419–4421 (1972).

45. R. M. Izatt, K. Pawlak, J. S. Bradshaw, R. L. Bruening, Thermodynamic and kinetic data for macrocycle interactions with cations and anions. *Chem. Rev.* **91**, 1721–2085 (1991).

46. Y. Takeda, Y. Kohno, Y. Kudo, N. Fukada, Stabilities in water and transfer activity coefficients from water to nonaqueous solvents of benzo-18-crown-6–metal ion complexes. *Bull. Chem. Soc. Jpn.* **62**, 999–1003 (1989).

47. S. Plimpton, Fast parallel algorithms for short-range molecular dynamics. *J. Comput. Phys.* **117**, 1–19 (1995).

48. S. Labík, W. Smith, Scaled particle theory and the efficient calculation of the chemical potential of hard spheres in the NVT ensemble. *Mol. Simulat.* **12**, 23–31 (1994).

49. N. S. Martys, R. D. Mountain, Velocity Verlet algorithm for dissipative-particle-dynamics-based models of suspensions. *Phys. Rev. E* **59**, 3733–3736 (1999).

50. R. Hockney, J. Eastwood, *Computer Simulation Using Particles* (CRC Press, 1988).

51. G. Kresse, J. Furthmüller, Efficiency of ab-initio total energy calculations for metals and semiconductors using a plane-wave basis set. *Comp. Mater. Sci.* **6**, 15–50 (1996).

52. G. Kresse, J. Furthmüller, Efficient iterative schemes for ab initiototal-energy calculations using a plane-wave basis set. *Phys. Rev. B* **54**, 11169–11186 (1996).

53. J. P. Perdew, K. Burke, M. Ernzerhof, Generalized gradient approximation made simple. *Phys. Rev. Lett.* **77**, 3865–3868 (1996).

54. P. E. Blöchl, Projector augmented-wave method. *Phys. Rev. B* **50**, 17953–17979 (1994).

55. S. Grimme, J. Antony, S. Ehrlich, H. Krieg, A consistent and accurate ab initio parametrization of density functional dispersion correction (DFT-D) for the 94 elements H-Pu. *J. Chem. Phys.* **132**, 154104 (2010).

56. G. Henkelman, H. Jónsson, Improved tangent estimate in the nudged elastic band method for finding minimum energy paths and saddle points. *J. Chem. Phys.* **113**, 9978–9985 (2000).

57. G. Henkelman, B. P. Uberuaga, H. Jónsson, A climbing image nudged elastic band method for finding saddle points and minimum energy paths. *J. Chem. Phys.* **113**, 9901–9904 (2000).

58. M. R. DeStefano, T. Islamoglu, S. J. Garibay, J. T. Hupp, O. K. Farha, Room-temperature synthesis of UiO-66 and thermal modulation of densities of defect sites. *Chem. Mater.* **29**, 1357–1361 (2017).

59. T. Qian, H. Zhang, X. Li, J. Hou, C. Zhao, Q. Gu, H. Wang, Efficient gating of ion transport in three-dimensional metal–organic framework sub-nanochannels with confined light-responsive azobenzene molecules. *Angew. Chem. Int. Ed.* **59**, 13051–13056 (2020).

60. R. M. Venable, Y. Luo, K. Gawrisch, B. Roux, R. W. Pastor, Simulations of anionic lipid membranes: Development of interaction-specific ion parameters and validation using NMR data. *J. Phys. Chem. B* **117**, 10183–10192 (2013).

61. S. H. Lee, J. C. Rasaiah, Molecular dynamics simulation of ionic mobility. I. Alkali metal cations in water at 25 °C. *J. Chem. Phys.* **101**, 6964–6974 (1994).

62. J. Abraham, K. S. Vasu, C. D. Williams, K. Gopinadhan, Y. Su, C. T. Cherian, J. Dix, E. Prestat, S. J. Haigh, I. V. Grigorieva, Tunable sieving of ions using graphene oxide membranes. *Nat. Nanotechnol.* **12**, 546–550 (2017).

63. F. Sheng, B. Wu, X. Li, T. Xu, M. A. Shehzad, X. Wang, L. Ge, H. Wang, T. Xu, Efficient ion sieving in covalent organic framework membranes with sub-2-nanometer channels. *Adv. Mater.* **33**, e2104404 (2021).

64. Z. Jia, Y. Wang, W. Shi, J. Wang, Diamines cross-linked graphene oxide free-standing membranes for ion dialysis separation. *J. Membr. Sci.* **520**, 139–144 (2016).

65. R. Joshi, P. Carbone, F.-C. Wang, V. G. Kravets, Y. Su, I. V. Grigorieva, H. Wu, A. K. Geim, R. R. Nair, Precise and ultrafast molecular sieving through graphene oxide membranes. *Science* **343**, 752–754 (2014).

66. Y.-H. Xi, Z. Liu, J. Ji, Y. Wang, Y. Faraj, Y. Zhu, R. Xie, X.-J. Ju, W. Wang, X. Lu, Graphene-based membranes with uniform 2D nanochannels for precise sieving of mono-/multi-valent metal ions. *J. Membr. Sci.* **550**, 208–218 (2018).

67. S. Li, J.-H. Lee, Q. Hu, T.-S. Oh, J.-B. Yoo, Scalable graphene composite membranes for enhanced ion selectivity. *J. Membr. Sci.* **564**, 159–165 (2018).

68. R. Tan, A. Wang, R. Malpass-Evans, R. Williams, E. W. Zhao, T. Liu, C. Ye, X. Zhou, B. P. Darwich, Z. Fan, Hydrophilic microporous membranes for selective ion separation and flow-battery energy storage. *Nat. Mater.* **19**, 195–202 (2020).

69. H. J. Cassady, E. C. Cimino, M. Kumar, M. A. Hickner, Specific ion effects on the permselectivity of sulfonated poly (ether sulfone) cation exchange membranes. *J. Membr. Sci.* **508**, 146–152 (2016).

70. A. Somrani, A. Hamzaoui, M. Pontie, Study on lithium separation from salt lake brines by nanofiltration (NF) and low pressure reverse osmosis (LPRO). *Desalination* **317**, 184–192 (2013).

71. A. Garifzyanov, N. Davletshina, A. Garipova, R. Cherkasov, Sinergetic membrane extraction of lithium ions with new organophosphorus carriers. *Russ. J. Gen. Chem.* **84**, 285–288 (2014).

72. J.-h. Song, H.-W. Yu, M.-H. Ham, I. S. Kim, Tunable ion sieving of graphene membranes through the control of nitrogen-bonding configuration. *Nano Lett.* **18**, 5506–5513 (2018).

73. E. Nightingale Jr., Phenomenological theory of ion solvation. Effective radii of hydrated ions. *J. Phys. Chem.* **63**, 1381–1387 (1959).

74. Y. Marcus, A simple empirical model describing the thermodynamics of hydration of ions of widely varying charges, sizes, and shapes. *Biophys. Chem.* **51**, 111–127 (1994).